Large eddy simulations of a triangular jet and its counterpart through a chamber

Large eddy simulations of a triangular jet and its counterpart through a chamber[*]

Xiu Xiao(肖秀)[1], Guo-Chang Wang (王国昌)[2], Min-Yi Xu(徐敏义)[1] and Jian-Chun Mi(米建春)[1,2†]

[1]*Marine Engineering College, Dalian Maritime University, Dalian 116026, China*
[2]*College of Engineering, Peking University, Beijing 100871 China*

A free triangular jet (TJ1) and its counterpart initially passing a short circular chamber (TJ2) are numerically modeled using Large Eddy Simulation (LES). This paper compares the near-field characteristics of the two jets in detail. To enable some necessary experimental validations, the LES conditions of TJ1 and TJ2 are taken to be identical to those measured by Xu et al. (Sci. China Phys., 56, 1176, 2013) and England et al. (Exp. Fluids. 48, 69, 2010), respectively. The LES predictions are found to agree well with those measurements. It is demonstrated that a strong swirl occurs near the chamber inlet plane for the TJ2 flow. At the center of the swirl, there is a cluster of three sink foci, where each focus is aligned midway between the original triangular apexes. In the vortex skeleton constructed from the time-averaged flow field, the vortices arising from the foci are helically twisted around the core of the jet. As the flow passes through the chamber, the foci merge to form a closed-loop "bifurcation line", which separates the inward swirling flow and the outward oscillating jet. This global oscillation is regarded as a source node near the centerline of the chamber. If the chamber is removed for a "free" jet, *i.e.* TJ1, a cluster of three pairs of counter-rotating foci is produced and the net swirl circulation is zero, so the overall oscillation of the jet does not occur.

Keywords: turbulent, triangular jet, large eddy simulation
PACS: 47.27.wg, 47.27.-i

1. Introduction

Turbulent jets play an important role in the fundamental research of jet flows and in industrial applications. Different from the traditional circular jets, the noncircular jets, such as the triangular jets, the elliptical and the rectangular jets, have advantages in entraining and mixing due to the curvature difference of the nozzle exit and the instability produced by the sharp corners.[1] Therefore, many researches have been conducted to clarify the flow-field characteristics of the noncircular turbulent jets over recent decades.[2-10] Significantly, Mi and Nathan[11] studied experimentally the centerline velocity characteristics of turbulent free jets issuing from nine differently-shaped nozzles at a Reynolds number of 15,000. The results showed that the jet from the isosceles triangular orifice produces the greatest decay rate in the near-field mean velocity of all the jets. By using TSI 2-D laser Doppler velocimetry (LDV), Iyogun and Birouk[12] investigated the turbulent free jets issuing from five different nozzle geometries, i.e. triangular, smooth pipe, rectangular, contracted circular and square. They found that the triangular jet exhibits the highest rate of entrainment and spreading among the five nozzles. Note that the combustion process requires not only large-scale mixing to promote the bulk mixing of fuel and oxidizer, but also small-scale mixing to facilitate chemical reactions.[13] The turbulent characteristics of triangular jets provide superior advantages for its application in combustion systems. Therefore, in this work, turbulent jets issuing from sharped-edged triangular nozzle are studied in detail.

'Axis-switching', which is the change of the cross-sectional shape caused by the asymmetric distributions of pressure and mean flow field, is a distinguish phenomenon in noncircular jets.[14] In the case of triangular free jets, the key features of the axis-switching have been observed, *e.g.*, by Gutmark and Grinstein[15] and Lindstrom and Amitay[16]. Lee[17] explained axis-switching in terms of self-induced motion of vortex lines in shear layer of a triangular jet. In essence, the triangular-jet shear layer exhibits a cluster of six counter-rotating longitudinal vortices. At midway between the apexes, the vortex-induced velocity points away from the center of the jet. At the corners, it points toward the center of the jet. The jet flow therefore spreads more from the flat sides than from the corners of the exit and so the minor and major

axes of the triangular jet would 'switch' places.[15]

The exit profile also plays an important role for the downstream development of the jet.[18] When a triangular jet passes through a short circular chamber, a partially-confined triangular jet is formed and likely to oscillate with respect to the chamber axis under some conditions.[19] The confinement of the chamber causes the TJ2 to reattach the inside surface, and in the region upstream of the reattachment, a strong swirling flow exists adjacent to the triangular inlet. It was postulated in reference [17] that the shear-layer interaction between the swirl and the jet should produce three co-rotating longitudinal vortices, which then merge to form a single vortex within the chamber. As a result, the TJ2 may oscillate continuously.[19]

To better understand the oscillation behavior, a more detailed flow field of TJ2 is needed to be visualized. This need however can be met only by direct numerical simulation (DNS) or large eddy simulation (LES). The instantaneous field measurements of velocity and vorticity are impossibly made experimentally inside the chamber. Xu et al.[20] performed LES for TJ2 flow and examined its mean and instantaneous characteristics. Yet, they did not investigate the presence of the chamber on the near-field characteristics of a triangular-jet flow, *i.e.* TJ2, against a "free" triangular jet TJ1. The present work by LES is designated to find the dynamic distinctions between TJ2 and TJ1 flows, which result from the presence of a circular chamber.

The rest of the paper is organized as follows. Section 2 describes the LES technique (Section 2.1) and the nozzle model used to obtain the flow simulation (Section 2.2). In Section 3, the numerical results are presented in the following manner: Section 3.1 discusses the validation of the LES data with available PIV measurements. This is followed by a presentation of flow-visualization results to identify the features of TJ1 and TJ2 flows, where Section 3.2 presents the longitudinal flow field and Section 3.3 presents the cross-stream flow field. This reveals the structure of the time-averaged oscillating flow inside the chamber. Details of the vortex structure are provided in Section 3.4. Key differences between the TJ1 and the TJ2 flows are summarized in Section 4.

2. Computational details

2.1. LES method

In LES modeling of the unsteady incompressible TJ1 and TJ2 flows, the following spatially-filtered governing equations are solved with constant density and kinematic viscosity of the fluid:

$$\frac{\partial \overline{u_i}}{\partial t} + \frac{\partial \overline{u_i u_j}}{\partial x_j} = -\frac{\partial \overline{p}}{\partial x_i} + \frac{1}{Re_1}\frac{\partial^2 \overline{u_i}}{\partial x_i \partial x_j} - \frac{\partial \tau_{ij}}{\partial x_j} \tag{1}$$

$$\frac{\partial \overline{u_i}}{\partial x_i} = 0 \tag{2}$$

where t represents time, x_i ($i = 1, 2, 3$) are the streamwise, crosswise and spanwise coordinates respectively, later replaced by (x, y, z); $\overline{u_i}$ is the corresponding spatially-filtered velocity component and $\overline{p}$ is the spatially-filtered pressure. The overbar denotes that a low-pass filter G_Δ is applied to the flow motion, where Δ is the width of the sub-grid-scale (SGS) filter. Then, the scales of motion are decomposed into a grid-scale part (e.g., $\overline{u_i}$ and $\overline{p}$) corresponding to scales larger than Δ and an SGS part corresponding to scales smaller than Δ. The former is directly solved while the latter requires modeling.

In Eq. (1), the SGS stresses τ_{ij} are unknown and need modeling. They are closed by employing the Boussinesq hypothesis[21], i.e.,

$$\tau_{ij} = \overline{u_i u_j} - \overline{u_i}\,\overline{u_j} \tag{3}$$

$$\tau_{ij} - \frac{\delta_{ij}}{3}\tau_{kk} = -2\nu_t \overline{S}_{ij} \tag{4}$$

where δ_{ij} is the Kronecker delta and ν_t is the eddy viscosity. The strain-rate tensor $\overline{S}_{ij}$ is defined as

$$\overline{S}_{ij} = \frac{1}{2}\left(\frac{\partial \overline{u_i}}{\partial x_j} + \frac{\partial \overline{u_j}}{\partial x_x} \right) \tag{5}$$

In this study, the dynamic Smagorinsky model[22,23] is adopted for the eddy viscosity,

i.e.,

$$\nu_t = C\Delta^2 \left| \overline{S} \right| \tag{6}$$

where C is the numerical coefficient dynamically computed in the LES calculation and $\left| \overline{S} \right| = \sqrt{2\overline{S}_{ij}\overline{S}_{ij}}$. The width of the SGS filter Δ is determined by the volume of the computational cell (i.e. $\Delta = V^{1/3}$). To obtain C, the flow field obtained by using the SGS filter Δ is compared with that obtained by using a coarser 'test' filter (e.g. $\hat{\Delta} = 2\Delta$). The difference between the two resolved flow fields is the contribution of the small scales, where the size of the small scales falls between that of the SGS filter and the test filter.

At the test-filter level, the stress tensor in Eq. (3) is rewritten as

$$T_{ij} = \widehat{\overline{u_i u_j}} - \hat{\overline{u}}_i \hat{\overline{u}}_j \tag{7}$$

It can be parameterized in a manner analogous to the relation describes in Eq. (4):

$$T_{ij} - \frac{\delta_{ij}}{3} T_{kk} = -2C\hat{\Delta}^2 \left| \hat{\overline{S}} \right| \hat{\overline{S}}_{ij} \tag{8}$$

where C is the same numerical coefficient defined in Eq. (6) and it is independent of the filtering process. The difference between the stress tensors in Eq. (3) and Eq. (7) is

$$L_{ij} = T_{ij} - \hat{\tau}_{ij} = \widehat{\overline{u}_i \overline{u}_j} - \hat{\overline{u}}_i \hat{\overline{u}}_j \tag{9}$$

where L_{ij} can be computed from the resolved large-eddy flow field. Substituting Eq. (4) and Eq. (8) into Eq. (9) yields the relation [20]:

$$C = \frac{(L_{ij} - L_{kk}\delta_{ij} / 3)}{M_{ij}M_{ij}} \tag{10}$$

where

$$M_{ij} = -2(\hat{\Delta}^2 \left| \hat{\overline{S}} \right| \hat{\overline{S}}_{ij} - \Delta^2 \widehat{\left| \overline{S} \right| \overline{S}_{ij}}) \tag{11}$$

For Eq. (10), it is known that the coefficient C varies with space (x, y, z) and time (t). However, a too large C may cause numerical instability and result in divergence. To ensure that the LES computation is stable and that the dynamics SGS stress model performs satisfactorily in near-wall regions, commercial software package such as 'Fluent' limits the local value to within the usual operating range $0 < C < 0.23$.[22]

The present work utilizes a finite volume method available in Fluent 6.3[24], following the same simulation protocol given by Xu et al.[20]. For example, the 'SIMPLEC' method is used for coupling the pressure and the velocity, the second-order three-level implicit scheme for the LES time step and the central difference scheme for a spatially-discretized nozzle model.

2.2. The nozzle model used for LES

For this simulation, both TJ1 and TJ2 nozzles have the same equivalent inlet diameter, i.e. $D_e = 7.6$ mm. The TJ2 chamber has a length of $L = 8.75D_e$ and a diameter of $D = 3.5D_e$. The lip diameter at the exit plane of the chamber is $d_2 = 2.87D_e$. The fully-developed turbulent pipe flow is set as the jet inlet condition with a flow profile matching an empirical $1/7^{\text{th}}$ power-law:[20, 25]

$$U(r) = U_{cl}\left(1 - \frac{2|r|}{D_0}\right)^{1/7} \tag{12}$$

where U_{cl} is the pipe centerline velocity and $U(r)$ is the streamwise component of the time-averaged velocity at the radial distance r from the centerline of the supply pipe with diameter D_0. To simulate the pipe flow, a typical random fluctuation of $0.01U(r)$ is assumed.[19] The orifice-inlet Reynolds number is $Re = U_e D_e/\nu = 1,7900$, where U_e is the mass-averaged velocity at the inlet orifice and ν is the kinematic viscosity of the fluid.
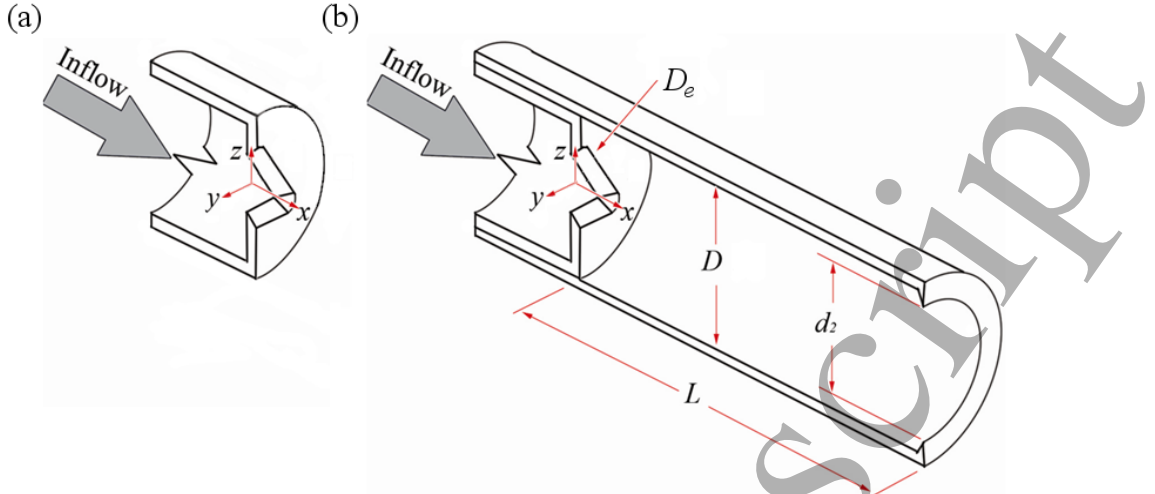
Fig. 1 Schematic diagram of (a) the TJ1 nozzle and (b) the TJ2 nozzle showing the geometric notations. Here D = $3.5D_e$, $L = 8.75D_e$, $d_2 = 2.87D_e$.
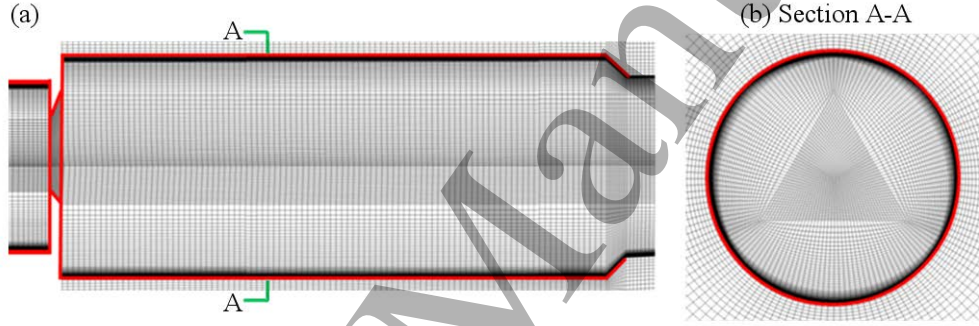

Fig. 2 Computational grid of the TJ2 nozzle in (a) the longitudinal section (xy plane at $z = 0$) and (b) the cross-section (yz plane at $x = D$) of the chamber.

Fig. 1 and Fig. 2 show the LES grid model for the TJ1 and TJ2 flow, respectively. For both jet flows, the computational domain has a large cylindrical "buffer" region ($30D_e$ in radius and $70D_e$ in length) which is concentric with the nozzle and begins immediately downstream of the triangular inlet orifice (e.g., see Fig. 2 of Xu et al.[20]). For the boundary of the nozzles and the ancillary component (i.e. the supply pipe), a no-slip condition was applied. For the boundary of the buffer region accompanying each nozzle, the conditions $\partial u_i/\partial r = 0$ (radial distribution), $\partial u_i/\partial x = 0$ (streamwise distribution) and $\overline{p} = 0$ (pressure distribution) were applied. A "Y-shaped" grid was used to construct a triangular mesh for the interior of the supply pipe and the nozzle. The triangular mesh could be divided into three quadrilaterals and so fully structured

hexahedral cell could be adopted.

To adequately simulate velocity gradients in the shear layer of the jet flow, it is necessary that the grid points are more densely spaced inside the chamber (for the TJ2) and adjacent to the corners of the triangle. The grid resolution Δ/D_e is 0.008 at the triangular inlet orifice. Moreover, the near-wall mesh is refined to capture the high shear in these regions. Calculation results show that $y^+ < 1$ in the boundary layer meshes, where y^+ is the dimensionless distance between the near-wall cell centroid and the boundary wall of the chamber and the inlet pipe, indicating the good performance of the present mesh. Finally, with 2 million grids for the present computational domain, the solution is sufficiently grid independent. This has been confirmed by initial checks, indicating that increasing the number of points by a factor of about 2 produces little change in the mean velocity field. To ensure that both jet flows achieve a steady-state solution, the independence of time step has been tested.[20] For the present simulation, an optimized time step of $t_s = 50$ μs is used to provide statistically independent samples (equivalent to $30000D_e/t_sU_e$) for the purpose of time-averaging the flow fields. For TJ2, the duration of sampling provides 60 cycles of large-scale jet oscillation.

3. Results and discussions

3.1. Validation of the LES modeling

To validate the simulations by experiment, Fig. 3 compares the LES-predicted mean velocities of the TJ1 and TJ2 on the centerline with those from the PIV measurements[25, 26] of a TJ1 at $Re = 50,000$ and a TJ2 at $Re = 17,900$. Of note, the LES and PIV data are normalized using the equivalent inlet diameter (D_e) and the inlet spatially averaged velocity (U_e). The triangular orifice is located at the origin $x=0$ and the exit plane of the TJ2 chamber is located at $x/D_e=8.75$. Note also that the values of U_{cl}/U_e for both TJ1 and TJ2 at $x/D_e=0$ are about 1.3. The values do not converge to 1.0 as the spatially averaged velocity U_e is lower than the centerline velocity U_{cl} for orifice jet flows. The available PIV measurements (Fig. 3) cover the downstream region $0 \leq x/D_e \leq 17$ for TJ1 and only $10 \leq x/D_e \leq 18$ for TJ2. The lack of

the measured data for $x/D_e \leq 10$ in TJ2 is because appropriate chamber-inside measurements are impossible, which is filled by the present LES calculation.
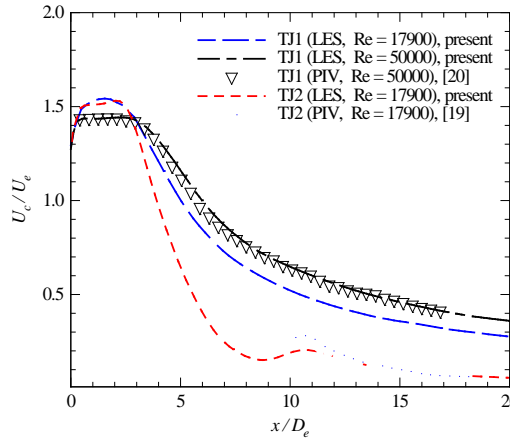

Fig. 3. Centerline mean velocities of TJ1 and TJ2 obtained from LES predictions and PIV measurements.

Manifestly, Fig. 3 displays a nearly perfect agreement between the LES and measured results for TJ1 at $Re = 50,000$. This has powerfully validated the LES effectiveness for the free jet. Despite so, there is a considerable difference in the decay rate of TJ1 between the cases for $Re = 17,900$ and $Re = 50,000$. This is likely due to a transition of the laminar-to-turbulent flow in the developing jet flow. In fact, the varying decay rates of axisymmetric turbulent free jets at moderate Re were reported by Mi et al.[27] and many others[28-30]. Fig. 3 also demonstrates the agreement between LES and the measured results at $10 \leq x/D_e \leq 18$ for TJ2 at $Re = 17,900$. Apparently, the LES simulation also works for the oscillating jet. Moreover, it is clearly shown that the triangular jet decays more rapidly when being initially confined by a chamber. This is because the induced large-scale jet oscillation occurs inside the chamber and accelerates the jet decay. Overall, as can be seen in Fig. 3, the LES simulations and the measurements are in close agreement, thus validating the LES modeling for the present study.

3.2. Visualization of the LES flow patterns

It has been difficult to visualize the TJ2 flow experimentally and careful reconstruction of the flow has required data from a large assortment of flow visualizations and measurements.[31] Since a complete set of experimental data to

disclose the TJ2 inside the chamber is impossible, the present LES data allows one to study in more detail the development of large-scale eddies in both the instantaneous and time-averaged flow fields. However, to acquire phase-averaged flow fields using LES presents a significant challenge due to highly aperiodic oscillation and characteristic low frequency of the TJ2.[25] In addition, there is a cost issue for a sufficiently long computational time that is necessary to attempt conditional averaging. The current LES approach therefore inevitably relies on visualizations of the instantaneous TJ1 and TJ2 to gain some understanding of their near flow field.
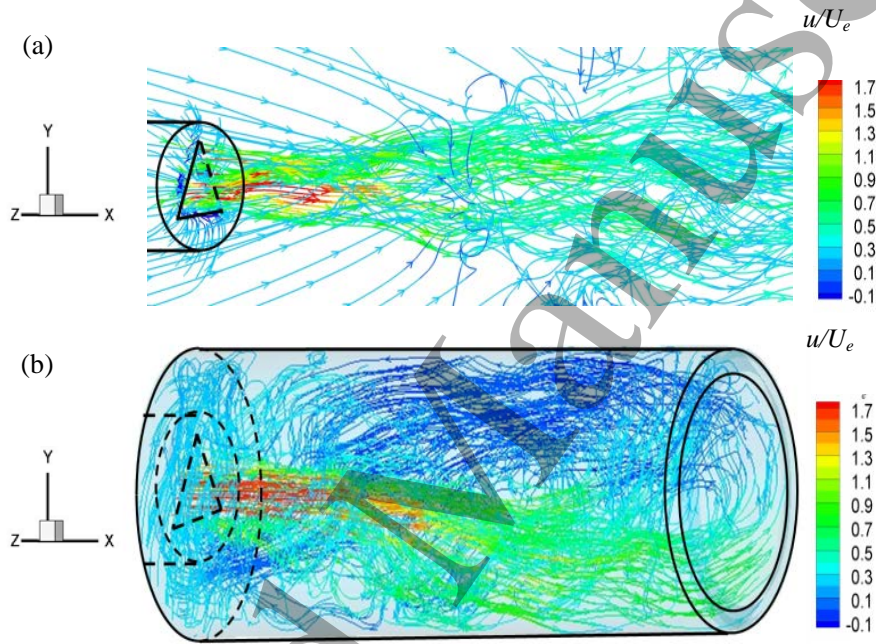
Fig. 4. Instantaneous three-dimensional streamline pattern of (a) the near-field flow of TJ1 and (b) the in-chamber flow of TJ2 at Re = 17,900. The streamlines are colored by normalized instantaneous streamwise velocity u/U_e.

Fig. 4 shows typical instantaneous streamline patterns in the near field ($0 \leq x/D_e \leq 9$) of the TJ1 and TJ2 flows. The instantaneous streamlines are shown in color to provide a sense of direction and magnitude of the local streamwise component of flow (u/U_e). For TJ1 without the chamber (Fig. 4(a)), the development of the jet flow is more straight forward. For example, the entrainment of ambient fluid by the jet flow is accompanied by a reduction in the jet (centerline) velocity and an increase in the half-width of the jet. This is consistent with the results presented in Ref. [26]. When a chamber is applied at the nozzle exit (i.e. TJ2 in Fig. 4(b)), the jet flow is highly

asymmetric. Specifically, the entrainment of ambient fluid into the chamber produces a large region of reverse flow that is not observed in the TJ1 flow. The ratio between the induced reverse flow rate into the chamber and the forward jet flow rate is about 0.12, see Ref. [20].

To visualize the shear layers of the TJ1 and TJ2 flows more clearly, the longitudinal cross-sections (in the xy plane) of the three-dimensional streamline patterns in Fig. 4 are displayed in Fig. 5. It can be seen from the instantaneous LES images (Fig. 4 and Fig. 5) that the large-scale eddies produced by the shear layers are highly unsteady. At the triangular inlet plane ($x = 0$), the jet flow clearly spreads faster at mid-way between the corners, and so the TJ2 has a high tendency of reattaching to the chamber wall in this azimuthal direction. Once jet reattachment is established in the chamber, the jet flow oscillates continuously. From a downstream view of the TJ2 flow in Fig. 4, the oscillation direction of the emerging jet is clockwise, see Fig. 13 of Xu et al. [20].
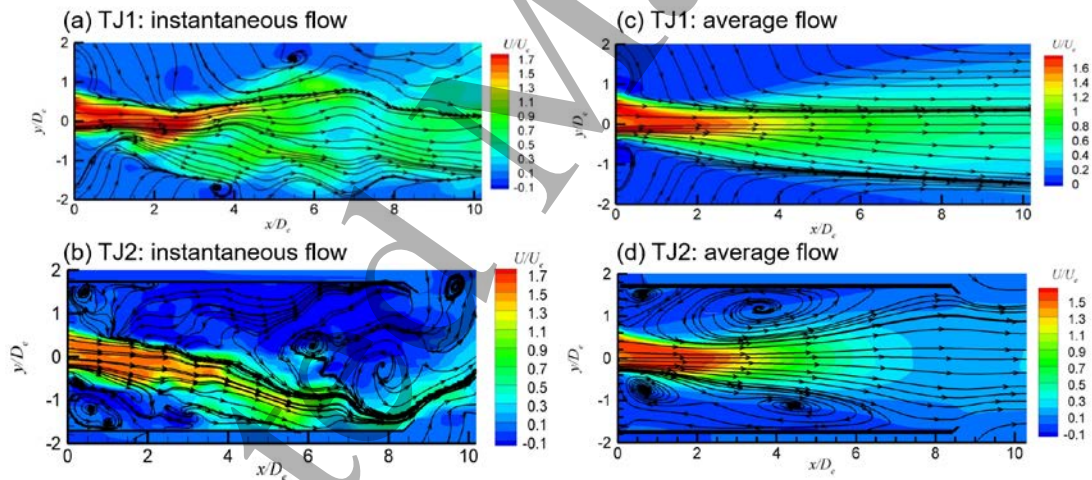

Fig. 5. Central xy-plane fields of the instantaneous (i.e. (a) and (b)) and time-averaged (i.e. (c) and (d))

longitudinal velocities of TJ1 and TJ2 flows.

For the TJ1 flow, the jet entrains ambient fluid in an axisymmetric manner and the spreading of the jet is accompanied by the decay in the streamwise velocity. As to the TJ2 flow, the reattachment phenomenon is accompanied by an asymmetric entrainment of the external ambient fluid and the eddies are larger than those of the TJ1 flow (see Fig. 5a and 5b). In the time-averaged flow field (Fig. 5c and 5d), the

large-scale eddies persist in the shear layer of the TJ2 (adjacent to the backward facing step), while for the TJ1, the shear layer is only visible as a longitudinal bifurcation line.

3.3. Cross-sectional flow field

Lee[17] suggested that vortex structure inside the chamber plays a key role in maintaining the TJ2 oscillation. Therefore, it seems useful to begin this section with a description of the vorticity field obtained from the present LES results. Figs. 6 and 7 show cross-sectional contours of the instantaneous and time-averaged streamwise vorticities of the TJ1 and TJ2 flows at several downstream locations side by side for comparison. The axial (x) component of vorticity is defined as

$$\omega_x = \frac{\partial W}{\partial y} - \frac{\partial V}{\partial z} \tag{13}$$

Streamlines are plotted together with the vorticity field for better understanding of the results. The streamlines (y_s, z_s) are obtained by integrating the expression

$$\frac{dy_s}{V} = \frac{dz_s}{W} \tag{14}$$

where $V(y)$ and $W(z)$ are the two crosswise velocity components, which provide information on critical points (e.g. nodes, saddles) and bifurcation lines in the flow field. From the LES data, the circulations of the jet flows can be determined by integrating vorticity over each selected cross-section (of area A), and the results are plotted against x/D_e in Fig. 8. Here, the positive circulation is defined by $\Gamma^+ = \iint \max(\omega_x, 0) dA$, the negative circulation is $\Gamma^- = \iint \min(\omega_x, 0) dA$ and the total circulation is the sum of the two quantities, i.e. $\Gamma = \Gamma^+ + \Gamma^-$.
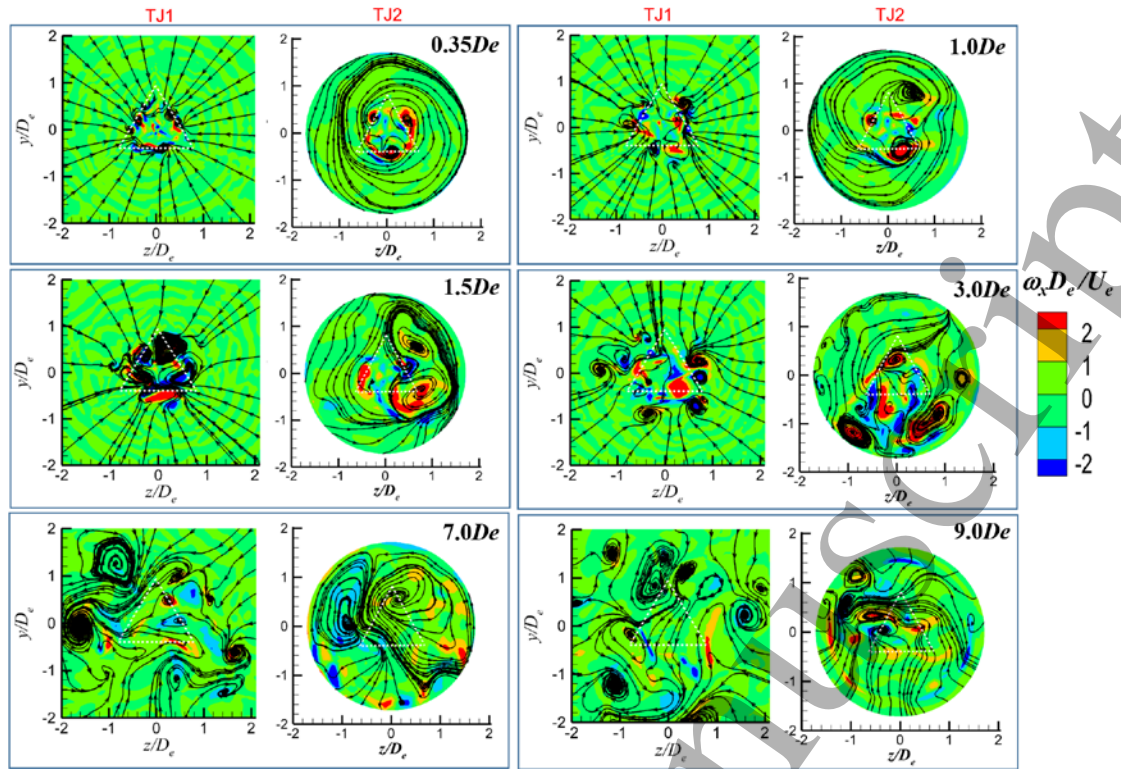
Fig. 6. Instantaneous vorticity contours and streamlines in cross-sections of TJ1 and TJ2 flows at different x/D_e.

It is evident from Fig. 7 that, starting from about $x/D_e = 1.0$, there are three pairs of counter-rotating foci in the TJ1 flow, where each pair is aligned midway between the corners of the triangular orifice. The vortices rising from the foci appear to evolve in a straightforward manner, where an increase in size of vortex is accompanied by a reduction of vorticity to maintain constant circulation (i.e. the Helmholtz vortex law). For the time-averaged TJ2 flow, a major feature is the presence of a strong inward counter-clockwise swirl around the inlet jet, see Fig. 7. Conversely, the precession of the TJ2 is in the clockwise direction. In the shear layer between the inlet jet and the swirling flow, there is a cluster of three co-rotating sink foci, which is resulted from the three original pairs of counter-rotating foci under the swirling flow. Both the swirl and the foci rotate in the same counter-clockwise direction. The vortices rising from the three foci are helically twisted around the core of the jet. They merge to form a closed-loop bifurcation line which separates the core flow and the inward swirling flow. The emerging core flow appears as a source node near the centerline of the chamber. At the exit plane of the chamber ($x/D_e = 9.0$), a closed-looped bifurcation line forms between the emerging flow and the induced ambient flow.
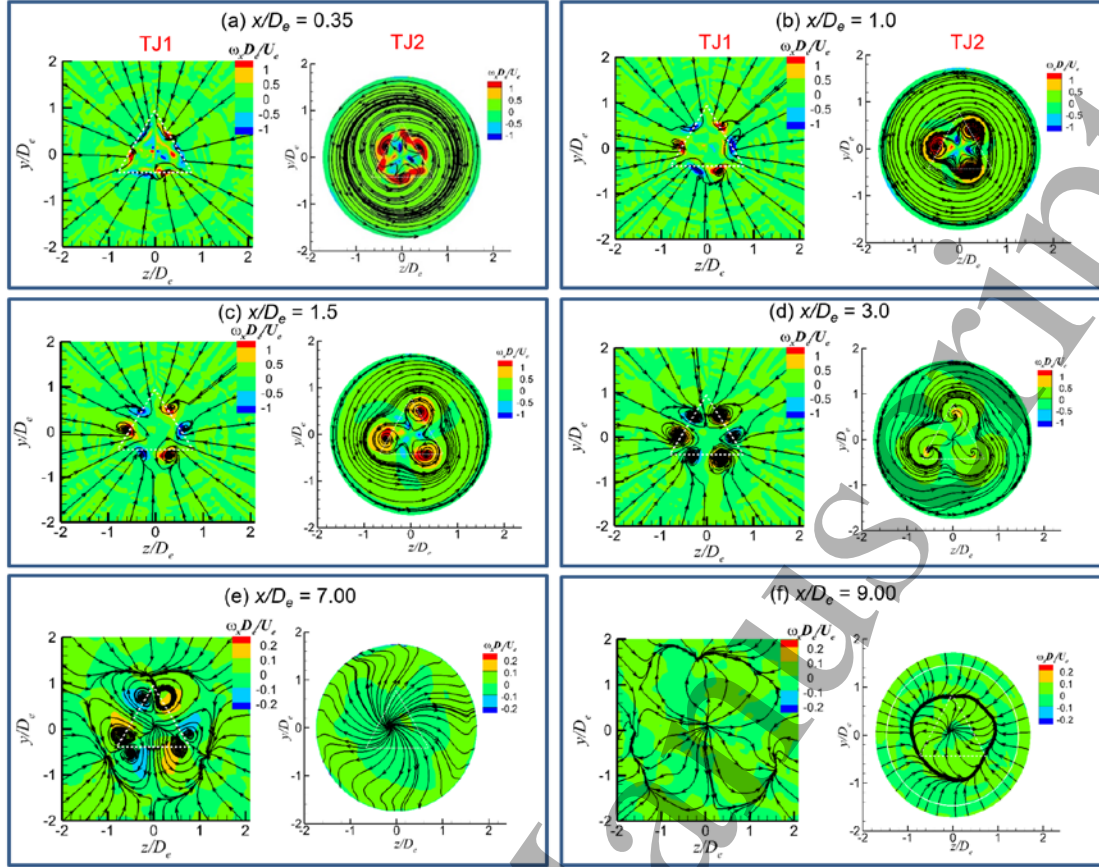
Fig. 7. Contours of the mean streamwise vorticity and streamlines in cross-sections of the TJ1 and TJ2 flows at different x/D_e.

As indicated in Fig. 6 and Fig. 7, the presence of the chamber clearly alters the vorticity field of the triangular-jet flow. This is further demonstrated in Fig. 8, where it can be seen that for the TJ1 and TJ2 flows, the positive Γ^+ and negative Γ^- contributions to the circulation Γ are very different. In the TJ2 flow, the Γ^+ and Γ^- are highly asymmetric due to the presence of swirl trapped by the chamber. The total circulation Γ is positive at $x/D_e < 2.4$ while it becomes negative at $x/D_e = 2.4\sim3.2$. The balance between Γ^+ and Γ^- is achieved further downstream. Note that the positive circulation ($\Gamma^+ > |\Gamma^-|$) in the TJ2 flow is indicative of the counter-clockwise swirling flow observed in Figure 7. The swirl is strongest at the inlet-end of the chamber ($x/D_e \leq 1$). If the chamber is removed, the jet flow has a three-fold axial symmetry with zero net circulation and the jet does not oscillate. Consequently, as shown in Fig. 8(b), along the axial direction of TJ1 flow, $\Gamma^+ = |\Gamma^-| \approx 0.375\pm0.075$.
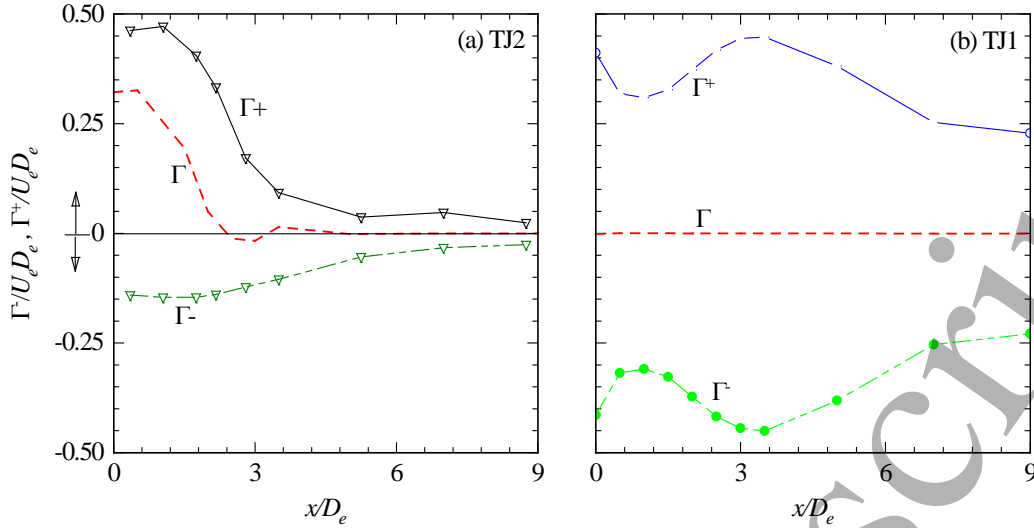
Fig. 8. The positive Γ^+/negative Γ^- contributions and the total circulation ($\Gamma = \Gamma^+ + \Gamma^-$) in the time-averaged (a) TJ2 and (b) TJ1 flows.

3.4. Vortex skeleton

From the vorticity distributions and streamline patterns of the TJ1 and TJ2 flows, Section 3.3 shows that there are strong vortex cores (i.e. sink foci) produced immediately downstream of the triangular inlet orifice. The next step is to visualize these structures using the 'Q-criterion' method of vortex identification, e.g., see Chakraborty et al. [32]. This method is based on the point-wise analysis of velocity gradient tensor. It defines a function that can be evaluated point-by-point and then classify each point as being inside or outside a vortex according to the criterion based on the point values. For the Q criterion, vortices are identified as flow regions with positive second invariant of the velocity gradient tensor,

$$Q = (\Omega_{ij}\Omega_{ij} - S_{ij}S_{ij})/2 > 0 \tag{15}$$

where $\Omega_{ij} = (u_{i,j} - u_{j,i})/2$ is the rate-of-rotation tensor and $S_{ij} = (u_{i,j} + u_{j,i})/2$ is the rate-of-strain tensor.[26] In an incompressible flow, Q provides a local measure of the excess rotation rate relative to the strain rate. It is more robust than the common intuitive measures of detecting vortices such as local pressure minima, spiraling streamlines and iso-vorticity surfaces.[33]
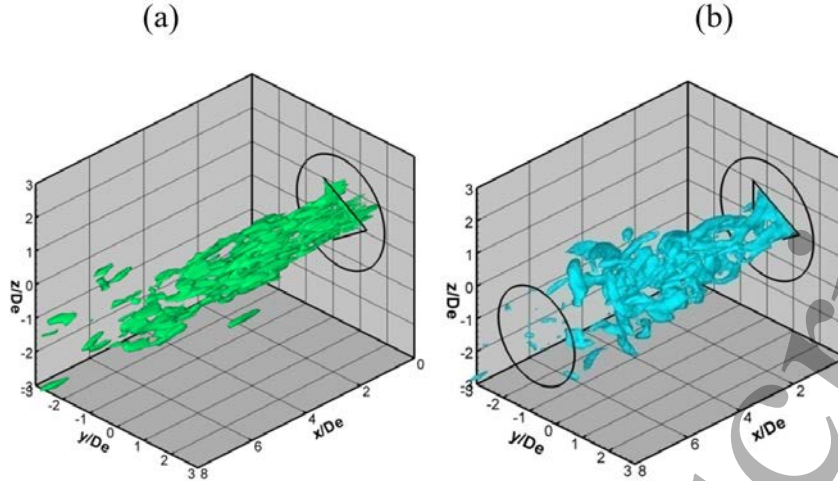
Fig. 9. Iso-surface of the normalized second invariant of the velocity gradient tensor for instantaneous (a) TJ1 and

(b) TJ2 flows at $Q^* = Q(U_e/D_e)^2 = 1.0$.

Fig. 9 shows typical examples of normalized instantaneous distributions at $Q^* = Q(U_e/D_e)^2 = 1.0$ for the two jet flows, where the dominant vortical structures have been identified with the Q^* criterion. The TJ1 flow structures have a slender appearance as they are predominantly stretched in the longitudinal direction (Fig. 9(a)). The TJ2 structures are comparatively larger than those of TJ1, despite it being confined in the chamber, and have a "spiral like" appearance due to the presence of swirl in the near-field surrounding secondary flow ($0 < x/D_e < 2$). In the near field of the TJ2 flow, three longitudinal vortices are produced at the triangular inlet orifice and they twist helically around the core of the jet (Fig. 9(b)).

The time-averaged distributions of Q^*, where the dominant (coherent) structures of TJ1 and TJ2 are more distinguishable, are shown in Fig. 10. By carefully selecting different positive values of Q^*, the vortex skeletons of the time-averaged TJ1 and TJ2 flows can be constructed and this should satisfy the first vortex law of Helmholtz. The law states that 'the circulation around a vortex tube is constant'.[34] As a consequence, vortex tubes in the ideal flow must form a closed loop, extend to infinity or terminate at solid surfaces. Fig. 10 shows that, for the given values of $Q^* = 0.01$, 0.02 and 0.05, the three pairs of counter-rotating vortex cores simply stretch downstream in the TJ1. For the TJ2, the vortex skeleton is larger in size with the vortex terminating (or breaks down) on the chamber wall. By increasing the value of Q^* from 0.01 to 0.05, the

time-averaged TJ2 flow shows two distinct structures: (i) the three co-rotating vortices near the triangular orifice are produced in the shear layer between the inlet jet and the swirl, and (ii) a closed vortex loop just upstream of the forward-facing exit lip is an artifact produced by the emerging deflected jet.
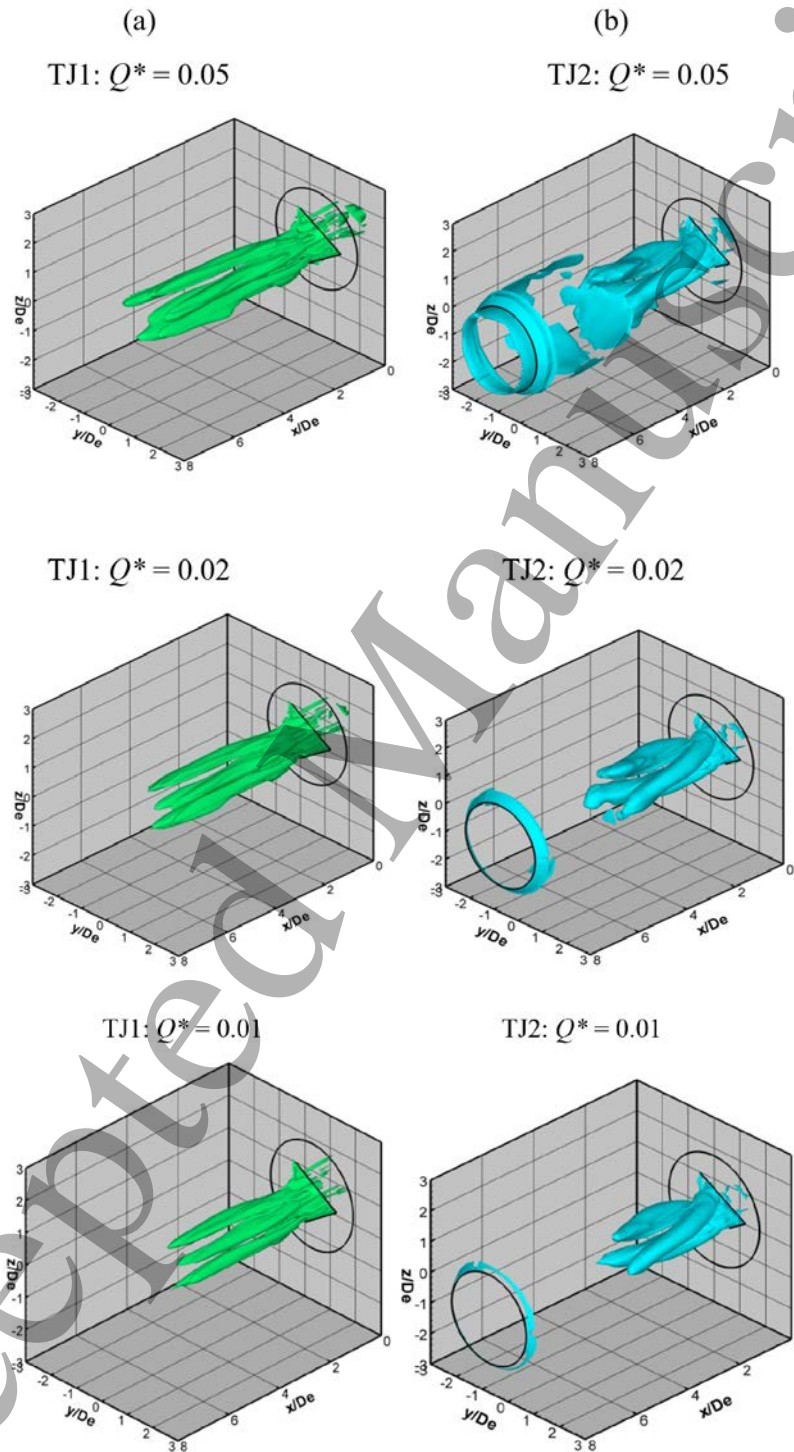

Fig. 10. Iso-surface of the normalized second invariant of the velocity gradient tensor for time-averaged (a) TJ1 and (b) TJ2 flows; Q* = 0.05, 0.02, 0.01.

To summarize, the three co-rotating vortices which swirl towards the chamber wall are present only in the TJ2 flow. This seems to be the key difference between the TJ2 and TJ1 flows. Swirl must be present near the triangular orifice in order to destabilize the corner vortices, and if there is no swirl or the net circulation is zero in the near field, the jet oscillation will not be produced.

4. Conclusions

The present work has performed the LES simulations of a free triangular jet and its counterpart through a short cylindrical chamber at Reynolds number of $Re =17,900$. The simulations show significant differences between the flow characteristics of the two jets. Specifically, the presence of the chamber induces a strong swirling flow around the jet just downstream of the chamber inlet and enables the three pairs of innate longitudinal vortices to spiral in the shear layer between the swirl and the jet. As a result, the emerging jet from the chamber outlet oscillates "spontaneously" in a large-scale fashion. In the time-averaged flow of the oscillating triangular jet (TJ2), the vortices merge to form a closed-loop bifurcation line, which separates the swirling flow and the emerging jet. In the constructed vortex skeleton of the TJ2 flow, the longitudinal vortices spiral and reattach to the cylindrical wall before emerging out from the chamber. If the chamber is removed, the flow returns to a conventional free jet, where there is no net swirl circulation and no large-scale oscillation to ensue.

The innovation of this work is to enable a better understanding of the TJ2 oscillation by visualizing the three-dimensional detailed flow field inside the chamber instantaneously, which cannot be made by experiment.

References
1. Gutmark E and Grinstein F F 1999 *Annu. Rev. Fluid Mech.* **31** 239
2. Schadow K C, Gutmark E, Parr D M and Wilson K J 1988 *Exp. Fluids* **6** 129
3. Rahman M S, Tay G F K and Tachie M F 2019 *Flow Turbul. Combust.* **103** 797
4. Hussain F and Husain H S 1989 *J. Fluid Mech.* **208** 257
5. Li Y, Li B, Qi F and Wang X 2017 *Chin. Phys. B* **26** 024701
6. Grinstein F F, Gutmark E and Parr T 1995 *Phys. Fluids* **7** 1483
7. Vouros A P, Panidis T, Pollard A and Schwab R R 2015 *Int. J. Heat Fluid Flow* **51** 383

8. Deo R C, Mi J and Nathan G J 2007 *Exp. Therm. Fluid Sci.* **32** 545

9. Xu M, Zhang J, Mi J, Nathan G J and Kalt P A M 2013 *Chin. Phys. B* **22** 034701

10. Shi X D, Feng L H and Wang J J 2019 *J. Fluid Mech.* **868** 66

11. Mi J and Nathan G J 2010 *Flow Turbul. Combust.* **84** 583

12. Iyogun C O, Birouk M 2009 *Flow Turbul. Combust.* **82** 287

13. Quinn W R 2005 *Exp. Fluids* **39** 111

14. Ghasemi A, Tuna B A and Li X 2019 *J. Fluid Mech.* **864** 141

15. Gutmark E and Grinstein F F 1999 *Annu. Rev. Fluid Mech.* **31** 239

16. Lindstrom A and Amitay M 2019 *AIAA J.* **57** 2783

17. Lee S K 2009 Study of a Naturally Oscillating Triangular-Jet Flow (PhD Thesis) (Adelaide: The University of Adelaide, Australia)

18. Zhang J, Xu M, Mi J 2014 *Chin. Phys. B* **23** 044704

19. Mi J, Nathan G J and Luxton R E U.S. Patent 6 685102 [2004]

20. Xu M, Mi J and Li P 2012 Flow Turbul. Combust. 88 367

21. Hinze J O 1975 *Turbulence* (McGraw-Hill Publishers)

22. Germano M, Piomelli U, Moin P and Cabot W H 1991 Phys. *Fluids A* **3** 1760

23. Lilly D K 1992 *Phys. Fluids A* **4** 633

24. Fluent 6.3 Documentation. Fluent Inc [2007]

25. England G, Kalt P A M, Nathan G J and Kelso R M 2010 *Exp. Fluids* **48** 69

26. Xu M, Zhang J, Mi J, Nathan G J and Kalt P A M 2013 *Sci. China Phys. Mech.* **56** 1176

27. Mi J, Xu M and Zhou T 2013 *Phys. Fluids* **25** 075101

28. Fellouah H, Pollard A 2009 *Phys. Fluids* **21** 115101

29. Sadeghi H, Lavoie P, Pollard A 2014 *J. Turbul.* **15** 335

30. Salkhordeh S, Mazumdar S, Jana A, Kimber M L 2019 *Flow Turbul. Combust.* **102** 559

31. Wong C Y, Nathan G J and Kelso R M 2008 *J. Fluid Mech.* **606** 153

32. Chakraborty P, Balachandar S and Adrian R J 2005 *J. Fluid Mech.* **535** 189

33. Jeong J and Hussain F 1995 *J. Fluid Mech.* **285** 69

34. Green S I 1995 *Fluid Vortices* (Kluwer Academic Publishers)